

# Materials Horizons

Accepted Manuscript

This article can be cited before page numbers have been issued, to do this please use: Z. Zeng, S. Kang, X. Jiang, H. Qiu, Y. Chang, Y. Chueh, L. Yuan, Y. Liang, J. Chang, G. Yang, S. Hung and C. Han, *Mater. Horiz.*, 2026, DOI: 10.1039/D6MH00152A.



This is an Accepted Manuscript, which has been through the Royal Society of Chemistry peer review process and has been accepted for publication.

Accepted Manuscripts are published online shortly after acceptance, before technical editing, formatting and proof reading. Using this free service, authors can make their results available to the community, in citable form, before we publish the edited article. We will replace this Accepted Manuscript with the edited and formatted Advance Article as soon as it is available.

You can find more information about Accepted Manuscripts in the [Information for Authors](#).

Please note that technical editing may introduce minor changes to the text and/or graphics, which may alter content. The journal's standard [Terms & Conditions](#) and the [Ethical guidelines](#) still apply. In no event shall the Royal Society of Chemistry be held responsible for any errors or omissions in this Accepted Manuscript or any consequences arising from the use of any information it contains.

## Atomically Dispersed Ru on Defective CdS for Photocatalytic Solar Fuel Production Coupled with Hydrazine Degradation

View Article Online  
DOI: 10.1039/D6MH00152A

This work demonstrates a novel dual-functional photocatalytic paradigm that couples efficient solar fuel production ( $H_2$  and  $CH_3OH$ ) with the complete degradation of the hazardous pollutant hydrazine ( $N_2H_4$ ), achieving a zero-carbon-emission process. This concept fundamentally diverges from conventional systems that rely on organic sacrificial agents (e.g., TEOA, alcohols), which inevitably generate carbonaceous byproducts ( $CO_2$ , formaldehyde) and complicate reaction mechanisms. The breakthrough is enabled by a rationally designed CdS-Ru catalyst, where sulfur vacancies and atomically dispersed Ru sites synergistically regulate directional charge transfer and optimize molecular adsorption, ensuring stoichiometric  $N_2H_4$  oxidation to  $N_2$  without ammonia byproducts. This strategy provides a transformative insight for materials science that it illustrates how engineering single-atom sites within defective semiconductors can create highly active redox centers to simultaneously drive two kinetically and thermodynamically distinct reactions, environmental remediation and clean fuel synthesis. It establishes a new design principle for multifunctional photocatalysts that address intertwined energy and environmental challenges, moving beyond the traditional paradigm of merely scavenging holes with sacrificial reagents.



The data supporting this article have been included as part of the Supplementary Information. View Article Online  
DOI: 10.1039/D6MH00152A  
Supplementary information: Tables S1-S7, Figure S1-S29, DFT computational method and further experimental details. See DOI: [URL – format <https://doi.org/DOI>]



## COMMUNICATION

# Atomically Dispersed Ru on Defective CdS for Photocatalytic Solar Fuel Production Coupled with Hydrazine Degradation

Zikang Zeng,<sup>a</sup> Siyu Kang,<sup>a</sup> Xiaohe Jiang,<sup>a</sup> Hai Qiu,<sup>b</sup> Yu-Chia Chang,<sup>c</sup> Yu-Ting Chueh,<sup>c</sup> Lan Yuan,<sup>\*b</sup> Yujun Liang,<sup>a</sup> Jianguo Chang,<sup>\*d</sup> Gui Yang,<sup>e</sup> Sung-Fu Hung<sup>\*c</sup> and Chuang Han<sup>\*a</sup>

Received 00th January 20xx,  
Accepted 00th January 20xx

DOI: 10.1039/x0xx00000x

## Abstract

Photocatalytic solar fuel production offers a sustainable approach for generating renewable feedstocks. However, this promising strategy is often hindered by the sluggish reaction kinetics and undesired CO<sub>2</sub> emission. In this study, we develop a CdS-Ru photocatalyst through the introduction of sulfur vacancy and atomically dispersed Ru sites into defective CdS. This design promotes directional charge transfer and forms highly active redox centers. Further leveraging the distinctive kinetic and thermodynamic features of hydrazine oxidation as a chemical regulation strategy, we establish a dual-functional paradigm that couples solar fuel production with hydrazine degradation. The CdS-Ru photocatalyst achieves hydrogen evolution and methanol production rates of 212.7 mmol g<sup>-1</sup> h<sup>-1</sup> and 1.4 mmol g<sup>-1</sup> h<sup>-1</sup>, respectively. It shows a substantial improvement over pristine CdS, and outperforms the systems employing conventional sacrificial reagents, such as triethanolamine or sulfides. Notably, this process yields no carbon-based byproducts (e.g., CO, CO<sub>2</sub>, and formaldehyde), ensuring a cleaner fuel production pathway. Comprehensive experimental analyses and theoretical simulations are conducted to elucidate the structural and electronic properties of the CdS-Ru catalyst, as well as the working mechanism of redox coupling, providing new insights for constructing dual-functional photocatalysts to tackle environmental and energy crises.

## New concepts

This work demonstrates a novel dual-functional photocatalytic paradigm that couples efficient solar fuel production (H<sub>2</sub> and CH<sub>3</sub>OH) with the complete degradation of the hazardous pollutant hydrazine (N<sub>2</sub>H<sub>4</sub>), achieving a zero-carbon-emission process. This concept fundamentally diverges from conventional systems that rely on organic sacrificial agents (e.g., TEOA, alcohols), which inevitably generate carbonaceous byproducts (CO<sub>2</sub>, formaldehyde) and complicate reaction mechanisms. The breakthrough is enabled by a rationally designed CdS-Ru catalyst, where sulfur vacancy and atomically dispersed Ru sites synergistically regulate directional charge transfer and optimize molecular adsorption, ensuring stoichiometric N<sub>2</sub>H<sub>4</sub> oxidation to N<sub>2</sub> without ammonia byproducts. This strategy establishes a new design principle for multifunctional photocatalytic system to address intertwined energy and environmental challenges, moving beyond the traditional paradigm of merely scavenging holes with organic sacrificial reagents.

## 1. Introduction

Solar-driven H<sub>2</sub>O splitting, CO<sub>2</sub> or N<sub>2</sub> reduction for the production of energy-rich chemicals, i.e., solar fuel production, has been widely regarded as a promising route to meet the growing global energy demand while mitigating environmental concerns.<sup>1</sup> However, the efficiency of solar-to-chemical energy conversion is significantly constrained by sluggish surface reaction kinetics on semiconductor materials.<sup>2,3</sup> In particular, the extraction and utilization of photoexcited holes typically occur at a much faster rate than the corresponding electron-driven photophysical and photochemical processes.<sup>4</sup> To reconcile the competing requirements of light absorption, charge carrier separation, and surface reaction kinetics, traditional photocatalytic systems often employ sacrificial agents such as triethanolamine (TEOA), ascorbic acid, sulfides, alcohols, and amines to scavenge photogenerated holes, as depicted in Scheme 1a.<sup>5,6</sup> Despite their widespread use, these scavengers still demand energetically favorable holes for oxidation and often lead to the generation of reactive

<sup>a</sup> Faculty of Materials Science and Chemistry, China University of Geosciences, Wuhan, 430074, China. E-mail: hanc@cug.edu.cn

<sup>b</sup> Key Laboratory of Hubei Province for Coal Conversion and New Carbon Materials, Wuhan University of Science and Technology, Wuhan, 430081, China. E-mail: yuanlan@wust.edu.cn

<sup>c</sup> Department of Applied Chemistry, National Yang Ming Chiao Tung University, Hsinchu, 300, Taiwan. E-mail: sungfuhung@nycu.edu.tw

<sup>d</sup> Faculty of Anhui Key Laboratory of Green Carbon Chemistry, Fuyang Normal University, Fuyang, 236037, China. E-mail: jgchang@fynu.edu.cn

<sup>e</sup> Faculty of Environmental Science and Engineering, Kunming University of Science and Technology, Kunming, 650500, China.



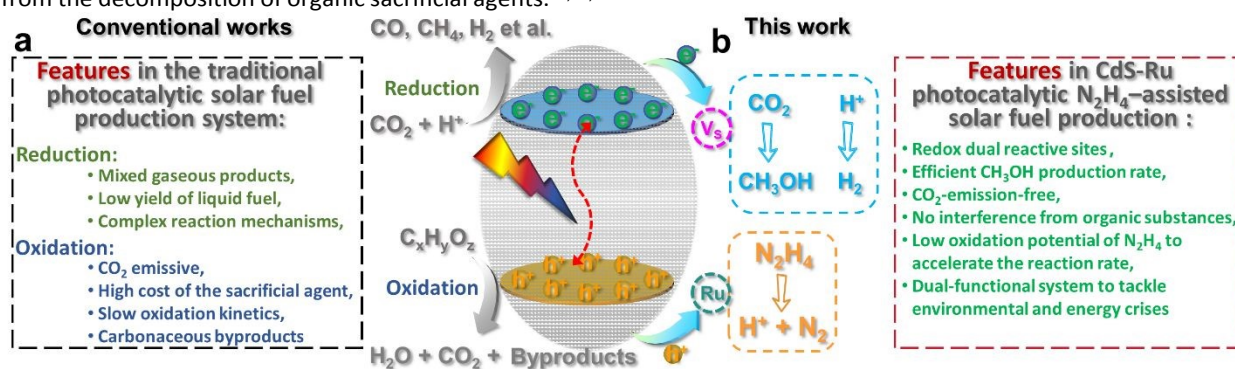
intermediates and carbonaceous byproducts,<sup>7</sup> including CO<sub>2</sub> and formaldehyde.<sup>8</sup> Such byproducts not only complicate the reaction mechanisms but also compromise the long-term stability of the semiconductor photocatalysts, thereby posing significant challenges to the development of durable and efficient photocatalytic systems.<sup>9,10</sup>

Ammonia (NH<sub>3</sub>), a readily oxidizable inorganic molecule with a high hydrogen storage density, has recently emerged as a promising hole scavenger for photocatalytic hydrogen production. Its low oxidation potential (+0.02 V vs. RHE) and the benign nature of its oxidation byproducts make it particularly attractive for sustainable applications.<sup>11</sup> However, hydrazine (N<sub>2</sub>H<sub>4</sub>) offers even greater potential due to its significantly lower oxidation potential (−0.33 V vs. RHE) and reduced tendency to poison catalysts.<sup>12</sup> These advantages have spurred increasing interest in employing the hydrazine oxidation reaction (HzOR) to replace the inherently sluggish water oxidation (+1.23 V vs. RHE) in electrocatalytic hydrogen production systems.<sup>13,14</sup> Moreover, hydrazine is a recognized environmental pollutant commonly detected in wastewater from the chemical, pharmaceutical, aerospace, and nuclear industries. Its high solubility (reaching 1400–1700 mg/L in certain industrial effluents),<sup>15, 16</sup> inherent alkalinity, and substantial chemical oxygen demand (COD) significantly complicate its removal from contaminated streams.<sup>17–20</sup> Although hydrazine commands a higher market price compared to conventional sacrificial agents or solar fuels (e.g., H<sub>2</sub>, methanol and NH<sub>3</sub>),<sup>13,14</sup> its status as a highly toxic and carcinogenic substance necessitates the urgent development of effective degradation strategies.<sup>17, 21, 22</sup> In this context, we propose that photocatalytic hydrazine decomposition represents a dual-purpose strategy, simultaneously enabling the environmentally responsible degradation of hazardous hydrazine and facilitating the generation of solar fuels (Scheme 1b). This approach not only enhances photocatalytic efficiency but also aligns with broader goals of environmental remediation and sustainable energy production.

The oxidation of hydrazine by photogenerated holes yields N<sub>2</sub> as the sole product, avoiding the emission of carbon-containing species such as CO, CO<sub>2</sub>, or formaldehyde. This eliminates complications in interpreting catalytic mechanisms that often arise from the decomposition of organic sacrificial agents.<sup>17,23,24</sup>

Particularly, carbonaceous oxidation can produce C1 or related products during photocatalytic CO<sub>2</sub> reduction, potentially resulting in ambiguous or overstated performance claims.<sup>25</sup> Additionally, the inherent alkalinity and low oxidation potential of hydrazine could enhance the solubility of CO<sub>2</sub> in aqueous media and help prevent over-oxidation of the reduction products.<sup>26</sup> Importantly, the resulting mixture of N<sub>2</sub> and solar fuels poses no significant safety risks. Indeed, the carbon-free feature of hydrazine already make it attractive in zero-carbon emission H<sub>2</sub> fuel production through electrocatalysis,<sup>27</sup> while hydrazine remains underexplored in photocatalytic systems.

Ruthenium (Ru) has demonstrated high activity for the hydrazine oxidation reaction (HzOR), primarily due to the strong orbital interaction between N 2p and Ru 3d orbitals.<sup>28</sup> However, conventional Ru nanoparticles often fail to achieve complete oxidation of hydrazine, leading to the formation of undesired byproducts such as ammonia.<sup>18</sup> Furthermore, given the limited availability and high cost of Ru, it is desired to develop photocatalysts with high mass activity to minimize the required loading of this noble metal.<sup>29,30</sup> In this sense, engineered Ru single-atom catalysts offer a promising strategy, as their excellent dispersion and full accessibility of active sites can significantly enhance photocatalytic efficiency.<sup>31</sup> Pioneering works suggested that transition metal sulfide semiconductors are promising platforms for engineering photocatalysts with atomically dispersed reactive sites,<sup>32–34</sup> due to the structure self-adapting reconstruction and defect-oriented coordination features. For instance, Liu et al. synergistically introduced S vacancy (V<sub>S</sub>) with atomic Cu into ZnIn<sub>2</sub>S<sub>4</sub> nanosheets to tune the charge separation and modulate gradient hydrogen migration for enhancing photocatalytic H<sub>2</sub> production.<sup>32</sup> Zhou et al. reported a strategy for modulating surface electron density and reactant adsorption manner by regulating a single Au atom in defective CdS for effective CO<sub>2</sub> photoreduction.<sup>35</sup> We envision that the dynamic charge transfer between isolated Ru atoms and the defective semiconductor substrate, along with the tunable coordination environment of Ru centers, can be leveraged to optimize the delocalized electron distribution and the adsorption behavior of hydrazine and related species. This, in turn, may facilitate the complete oxidation of hydrazine and improve overall solar fuel production performance.



**Scheme 1.** (a) Features of traditional photocatalytic solar fuel production system. (b) Features of CdS-Ru photocatalytic N<sub>2</sub>H<sub>4</sub>-assisted solar fuel production system.

Herein, we developed a photocatalytic system by incorporating atomically dispersed Ru into a defective CdS semiconductor (CdS-Ru) to enable zero-carbon-emission solar

fuel production via coupled hydrazine degradation. CdS was selected to be a model semiconductor due to its simple structure, readily accessible vacancies, and favorable visible



light harvesting. A combination of experimental investigations and density functional theory (DFT) calculations revealed that interfacial charge transfer and optimized molecular adsorption, regulated by  $V_S$  and atomically dispersed Ru active sites, play key roles in facilitating the complete dehydrogenation of hydrazine. This process results in the stoichiometric generation of reductive products ( $H_2$  or  $CH_3OH$ ) and the oxidative product ( $N_2$ ). The rationally designed CdS-Ru catalyst and the comprehensive investigation of its catalytic behavior in hydrazine-assisted solar fuel production offer valuable insights into the photocatalytic elimination of nitrogen-based pollutants and the development of clean energy production technologies.

## 2. Experimental section

### 2.1. Synthesis of CdS and CdS-Ru

Uniform CdS nanowires (NWs) were prepared through a solvothermal method.<sup>36</sup> The detailed processes were described in supporting information. Atomically dispersed Ru-modified CdS (CdS-Ru) was synthesized via a facile wet-chemical process, as depicted in Fig. 1a. Specially, cadmium diethyldithiocarbamate ( $Cd(S_2CNET_2)_2$ ) was firstly prepared by precipitating the mixture of sodium diethyldithiocarbamate trihydrate (DDTC) and cadmium chloride ( $CdCl_2$ ) in deionized water. Then 0.843 g  $Cd(S_2CNET_2)_2$  and a certain amount of  $RuCl_3 \cdot 3H_2O$  was added to a 50 mL capacity Teflon-lined stainless steel autoclave, followed by filling the autoclave with 30 mL of diethylamin. The autoclave was maintained at 180 °C for 24 h and subsequently cooled to room temperature. The resulting yellow precipitate was collected and washed with anhydrous ethanol and deionized water to remove residual organic solvents. The final product was dried in an oven at 60 °C for 12 h. The actual content of Ru (wt.%) in different samples was checked through inductively coupled plasma-mass spectrometry (ICP-MS, Agilent 7900) and the results are shown in Table S1. Since the photocatalytic activity of CdS-Ru<sub>0.18</sub> is highest among these samples, without special mention, the CdS-Ru refers to CdS-Ru<sub>0.18</sub> sample in the subsequent discussion.

### 2.2 Photoactivity test

The photocatalytic  $H_2$  production tests were conducted in a 50 mL quartz reactor equipped with circulating condensate water (10 °C), with a solvent of 10 mL aqueous solution of different concentrations (wt.%) of hydrazine hydrate, and a certain amount of catalyst was added to the solution system. After ultrasound dispersion, the reaction tube was purged with argon gas for 15 minutes to remove air, and then transferred to illumination under light emitting diode (LED,  $\lambda > 400$  nm, 60 mW  $cm^{-2}$ ) lamp or 300 W Xe ( $\lambda > 420$  nm, 200 mW  $cm^{-2}$ ) lamp to investigate the photocatalytic  $H_2$  production performance of the catalyst under weak and strong light conditions. The rotational speed was fixed at 500 rpm during testing. The produced gas was analyzed using gas chromatography. For

stability testing, the recovered catalyst was filtered using nylon filter paper and then dried at 60 °C. DOI: 10.1039/D6MH00152A

For  $CO_2$  photoreduction, 2 mg of catalyst and 10 mL of distilled  $H_2O$  containing 2 wt.% hydrazine hydrate were mixed in a quartz reactor (25 mL) equipped with circulating condensate water (10 °C) to form suspensions. The suspension was then purged with  $CO_2$  (or Ar) gas for 10 min. A Xe lamp ( $\lambda > 420$  nm) was used as the irradiation source. The energy output is 200 mW  $cm^{-2}$  measured by an optical power/energy meter (Newport 842-PE). During photocatalysis, the suspension was continuously stirred to ensure uniform irradiation. The evolved gases were analyzed using a gas chromatograph (Shimadzu GC-2014C, MS-5 A column, Ar carrier) equipped with a thermal conductivity detector (TCD) and a flame ionization detector (FID). Products in solution were analyzed on a gas chromatograph (Shimadzu GC-2014C, GDX-502 column, Ar carrier) and quantified using a Shimadzu TQ8040 gas chromatography-mass spectrometry (GC-MS). The liquid products were also qualitative by nuclear magnetic resonance (NMR, Bruker Avance, 600 MHz). The selectivity of  $CH_3OH$  was calculated according to the following formula:<sup>37</sup>

$$CH_3OH \text{ selectivity (\%)} = \frac{n(CH_3OH)}{n(CO) + n(CH_3OH)} \times 100\%$$

## 3. Results and discussion

### 3.1 Preparation and structure characterizations

Atomically dispersed Ru-modified CdS (CdS-Ru) was synthesized via a facile two-step process, as depicted in Fig. 1a. The CdS precursor exhibited an irregular lump-like morphology (Fig. S1), whereas both CdS and CdS-Ru showed uniform one-dimensional (1D) nanowire (NW) structures with an average diameter of approximately 40 nm, as confirmed in Fig. 1b and further detailed in Fig. S2. The length of NWs was extended to several micrometers. High-resolution transmission electron microscopy (HRTEM) characterization of CdS-Ru revealed well-defined lattice fringes with a spacing of 0.34 nm, corresponding to the (002) crystal plane of hexagonal CdS (Fig. 1c). Notably, no Ru/Ru<sub>x</sub> nanoparticles or nanoclusters were observed on the surface of CdS NWs, even in the sample with the highest Ru doping content (Fig. S2-4). Elemental mapping of Ru (Fig. 1d, Fig. S3 and S4) confirmed its uniform distribution, suggesting a high degree of atomic dispersion. Aberration-corrected high-angle annular dark field scanning TEM (HAADF-STEM) was employed (Fig. 1e), revealing that the ordered arranged metal atoms have different brightness.<sup>38</sup> The line-intensity profile marked with blue shows that Ru atoms appear on Cd atom row arrays (Fig. 1f), which indicates that Ru atom is replacing the Cd site of CdS.<sup>39</sup> The substitutional structure was further jointly corroborated by the following X-ray diffraction (XRD), electron paramagnetic resonance (EPR), and X-ray absorption spectroscopy (XAS) measurements.



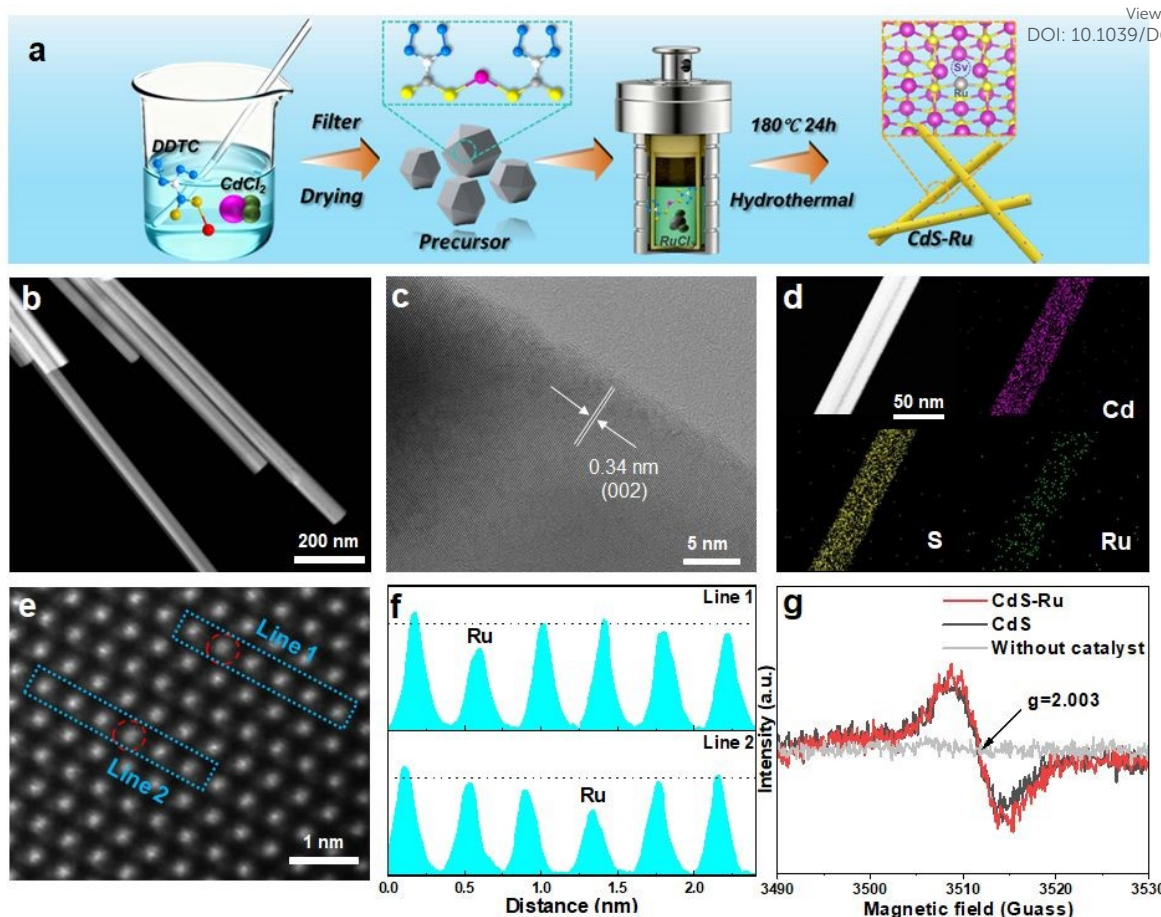


Fig. 1. (a) Schematic illustration of the synthesis of CdS-Ru. (b) TEM, (c) HRTEM, (d) elemental mapping and (e) aberration-corrected HAADF-STEM images of CdS-Ru. (f) Corresponding line-scan profiles marked in (e) with line 1 and line 2. (g) EPR curves of CdS, CdS-Ru and background.

The crystal structures of CdS and CdS-Ru were determined by X-ray diffraction (XRD). All samples exhibited diffraction patterns corresponding exclusively to the hexagonal CdS phase (PDF#41-1049), as shown in Fig. S5. A comparison of the XRD peak positions between CdS and CdS-Ru with different Ru loading contents reveals a slight negative shift upon Ru incorporation (Fig. S6), which can be attributed to lattice distortions induced by the embedded Ru species.<sup>32</sup> Electron paramagnetic resonance (EPR) measurements further confirmed structural modifications, with a pronounced signal at  $g = 2.003$  in both CdS and CdS-Ru, characteristic of  $V_S$  (Fig. 1g).<sup>32</sup> Given the similar ionic radii of Ru and Cd, the incorporation of Ru into the CdS lattice is expected to cause only modest structural perturbations, consistent with the slightly enhanced EPR signal intensity observed for CdS-Ru. This suggests that atomically dispersed Ru and sulfur vacancies coexist in the catalyst, collectively contributing to the modification of the local electronic structure. X-ray photoelectron spectroscopy (XPS) was employed to characterize the elemental composition and electronic interactions. The survey spectra confirmed the presence of Cd and S in both CdS and CdS-Ru (Fig. 2a). High-resolution XPS of Cd 3d (Fig. 2b) and S 2p (Fig. 2c) confirm the expected oxidation states of  $Cd^{2+}$  and  $S^{2-}$  in the CdS lattice. The slightly higher intensity observed for CdS-Ru, combined with the

positive shifts in Cd 3d and S 2p binding energies after Ru incorporation, suggests that Ru atoms substitute into the CdS lattice and modulate the local electronic environment, with sulfur vacancies present in the vicinity. Although the Ru signal in CdS-Ru is weak due to the low content and atomic dispersion of Ru (Fig. S7), the observed positive shifts in the binding energies of both Cd and S after Ru incorporation indicate a strong electronic interaction between Ru atoms and the CdS matrix.<sup>40</sup>

To further elucidate the structure and coordination environment of the Ru species in CdS-Ru, X-ray absorption spectroscopy (XAS) was performed. X-ray absorption near-edge structure (XANES) analysis (Fig. 2d) indicates that the average oxidation state of Ru in CdS-Ru lies between that of metallic Ru (Ru foil) and the  $Ru^{4+}$  in  $RuS_2$ , suggesting a partially oxidation state for the atomically dispersed Ru species.<sup>31</sup> The Fourier transform of the extended X-ray absorption fine structure (EXAFS) spectra (Fig. 2e) shows a prominent peak at  $1.84 \text{ \AA}$ , which can be ascribed to the Ru-S coordination bond.<sup>41</sup> Notably, there is no observable peak corresponding to Ru-Ru bonding ( $2.39 \text{ \AA}$ ), providing strong evidence for the atomic dispersion of Ru within CdS matrix. Quantitative EXAFS fitting (Fig. 2f and Table S2) estimates the Ru-S coordination number to be ca. 3, suggesting that each Ru atom is coordinated to three



sulfur atoms. Wavelet transform (WT) EXAFS analysis further corroborates this finding. The dominant WT intensity for CdS-Ru appears at  $8.0 \text{ \AA}^{-1}$  (Fig. 2g-i), positioned between the reference signals of Ru foil and  $\text{RuS}_2$ . This spatial frequency is

characteristic of Ru-S coordination and visually confirms the absence of Ru-Ru interactions, reinforcing the conclusion that Ru species are atomically dispersed on the CdS support.<sup>42</sup>

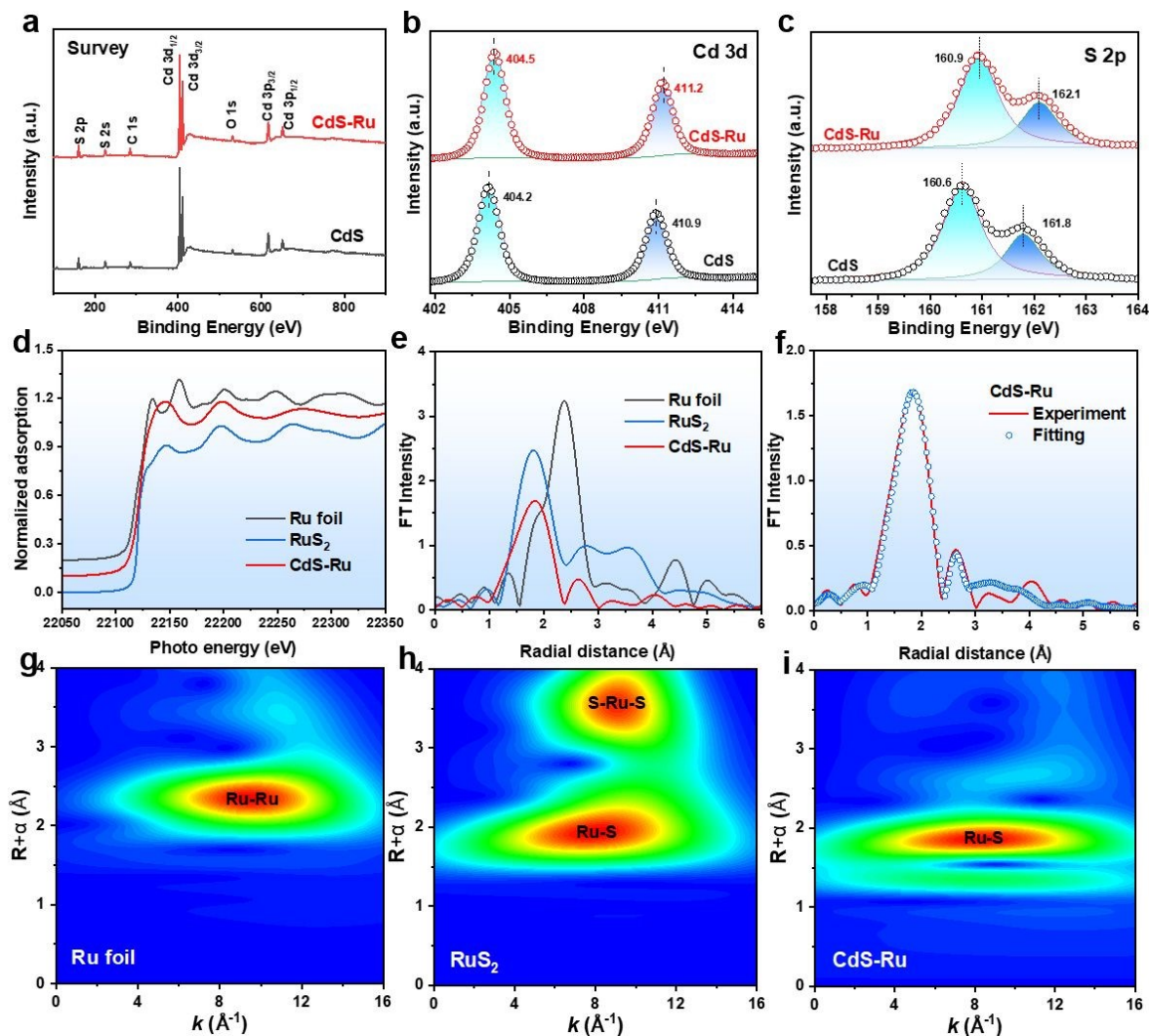


Fig. 2. (a) XPS survey spectrum for CdS and CdS-Ru. (b) High-resolution XPS spectra of Cd 3d and (c) S 2p spectra in CdS and CdS-Ru. (d) XANES and (e) EXAFS spectra of CdS-Ru (Ru foil and  $\text{RuS}_2$  were applied for comparison). (f) Fit of the EXAFS signals of CdS-Ru at the Ru R edge. (g-i) Wavelet transform of the  $k^3$ -weighted EXAFS signal at Ru K-edge of Ru foil,  $\text{RuS}_2$  and CdS-Ru.

### 3.2 Photocatalytic solar fuel production coupled with hydrazine degradation

The photocatalytic performance of CdS-Ru was evaluated separately in terms of both  $\text{H}_2$  evolution and  $\text{CO}_2$  reduction. The photocatalytic performance of  $\text{H}_2$  evolution coupled with hydrazine degradation was initially evaluated for CdS and CdS-Ru samples with varying Ru loading. As shown in Fig. S8, the CdS-Ru loaded with 0.18 wt.% Ru disclosed the highest  $\text{H}_2$  production rate, benefiting from the efficient separation and transfer efficiency of charge carriers, as will be discussed later. After further optimizing reaction conditions (Fig. S9), including hydrazine concentration and catalyst feeding, the CdS-Ru sample achieved a maximum  $\text{H}_2$  production rate of  $46.1 \text{ mmol g}^{-1} \text{ h}^{-1}$  under  $60 \text{ mW cm}^{-2}$  white light emitting diode illumination (LED,  $\lambda > 400 \text{ nm}$ ). This rate is 46 times higher than that of pristine CdS, which produced only  $1.0 \text{ mmol g}^{-1} \text{ h}^{-1}$ . To

check whether the  $\text{H}_2$  evolution process is driven by photocatalysis, controlled experiments were conducted. As shown in Fig. 3a and Fig. S10, the  $\text{H}_2$  evolution over CdS-Ru increases steadily during continuous light irradiation. No  $\text{H}_2$  generation was observed in the absence of either light or catalyst. In addition, using an equal molar amount of  $\text{RuCl}_3$  as that in CdS-Ru for the reaction leads to no  $\text{H}_2$  production (Fig. S11), confirming that the enhanced activity is both photocatalytic and catalyst-dependent. The apparent quantum efficiency (AQE) of CdS-Ru correlates well with its optical absorption spectrum (Fig. 3b), reinforcing that  $\text{H}_2$  evolution is driven by photoexcitation. The highest AQE, recorded at  $420 \text{ nm}$ , reached 31.79%.

Recyclability tests demonstrated that CdS-Ru shows a stable  $\text{H}_2$  evolution rate over multiple consecutive cycles (Fig. 3c), indicating excellent durability. Additionally, the sample stored



in-situ for 7 and 14 days retained its catalytic activity upon re-exposure to reaction conditions. Similar results were also observed in recycling tests performed under ambient conditions (Fig. S12). Post-reaction analyses, including structural (Fig. S13a), morphological (Fig. S13b and S13c), and composition (Fig. S14a and S14b) characterizations, confirmed that the CdS-Ru catalyst remained unchanged, further evidencing its structural stability and robustness. Although trace amounts of Cd–O or Cd–OH species might be formed on the catalyst surface after prolonged reaction, their concentration is below the detection limit of XPS and thus not observable in the Cd 3d spectrum. XANES and EXAFS analyses were performed on the Ru sites after the reaction. As shown in Fig. S15, the coordination environment of Ru remained largely unchanged after the reaction, while a slight positive shift in oxidation state was observed, which can be attributed to hole accumulation at the Ru sites due to the occurrence of reduction reactions. ICP-MS analysis of the recovered CdS-Ru after seven cycles (35 h) showed that the Ru content remained 0.18 wt.% (Table S3), identical to the fresh catalyst, and the reaction solution contained only 0.008 mg/L Cd, corresponding to dissolution of merely 0.005% of the total CdS. This trace Cd

leaching is attributed to the gradual consumption of hydrazine, which serves as the hole scavenger. After 35 h of cycling, approximately 25.8% of the initial hydrazine (51.7 mg out of 200 mg) is consumed. As the concentration of hydrazine decreases, a fraction of photogenerated holes cannot be promptly quenched, leading to mild photooxidation of the CdS lattice and resulting in trace Cd<sup>2+</sup> release. Furthermore, ICP-MS analysis of the reaction solution after a single 5 h photocatalytic cycle revealed a cadmium leaching concentration below 0.001 mg/L, which is within the WHO guideline limit for drinking water (< 0.003 mg/L).<sup>43</sup> After seven consecutive cycles over 14 days (total 35 h of reaction), the cumulative cadmium concentration reached 0.008 mg/L. No detectable ruthenium leaching was observed. While these results confirm good stability under typical operating conditions, prolonged use of CdS-based photocatalysts may lead to cumulative cadmium release, underscoring the need for developing cadmium-free alternatives. The inhibition of photocorrosion and good stability of CdS-Ru may be benefited from the relatively lower oxidation potential and carbon-free features of hydrazine, which hinder the generation of oxidative and poisonous species.

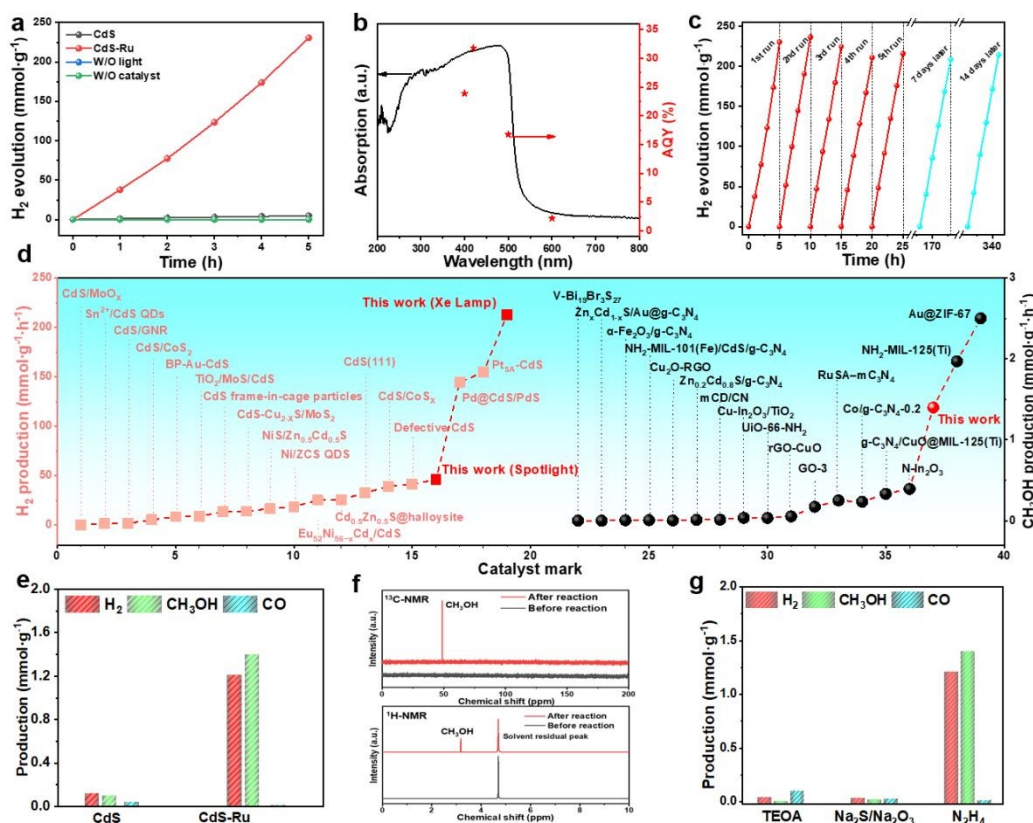


Fig. 3. (a) H<sub>2</sub> evolution performance of different photocatalysts under LED light irradiation (60 mW cm<sup>-2</sup>, λ > 400 nm) or dark conditions. (b) AQE testing for H<sub>2</sub> evolution over CdS-Ru. (c) The stability testing of CdS-Ru for photocatalytic H<sub>2</sub> evolution. Reaction conditions in a-c: 2 mg catalyst, 10 mL 2 wt.% hydrazine hydrate. (d) Comparison of H<sub>2</sub> and methanol production activity over different photocatalysts. The detailed information corresponding to different catalyst marks was disclosed in Tables S3 and S4. (e) The photocatalytic CO<sub>2</sub> reduction performance of CdS-Ru and CdS under Xe lamp (200 mW cm<sup>-2</sup>, λ > 420 nm). Reaction conditions: 2 mg catalyst, 10 mL 2 wt.% hydrazine hydrate. (f) <sup>13</sup>C-NMR and <sup>1</sup>H-NMR spectra before and after the photocatalytic CO<sub>2</sub> reduction with CdS-Ru. (g) Photocatalytic CO<sub>2</sub> reduction with CdS-Ru and different sacrificial agents.

To further highlight the advantages of CdS-Ru, in-situ photodeposition of Ru and Pt onto CdS was performed, a widely

recognized benchmark method for preparing efficient photocatalysts for H<sub>2</sub> evolution.<sup>44</sup> As shown in Fig. S16, CdS-Ru



significantly outperforms both Ru- and Pt-photodeposited CdS samples in terms of H<sub>2</sub> generation rate, demonstrating the superior catalytic efficiency of atomically dispersed Ru sites. Moreover, control experiments were conducted to evaluate H<sub>2</sub> evolution activity in the presence of alternative sacrificial agents, including CH<sub>3</sub>OH, TEOA, and Na<sub>2</sub>S/Na<sub>2</sub>SO<sub>3</sub> (Fig. S17). Among these, the hydrazine-assisted system showed the highest photoactivity, indicating its effectiveness as a hole scavenger. Collectively, these results confirm the synergistic effect between atomically dispersed Ru sites and hydrazine in enhancing H<sub>2</sub> evolution performance, supporting the rational design of the CdS-Ru system for efficient photocatalytic solar fuel production.<sup>19</sup>

For a more comprehensive comparison with other catalysts, the photocatalytic performance of CdS-Ru was further evaluated under a Xe lamp (200 mW cm<sup>-2</sup>, λ > 420 nm) or natural sunlight (Fig. S18). The H<sub>2</sub> evolution rates were measured to be 212.7 mmol g<sup>-1</sup> h<sup>-1</sup> and 60.2 mmol g<sup>-1</sup> h<sup>-1</sup> under Xe lamp and natural sunlight, respectively. Notably, the H<sub>2</sub> production rates achieved by CdS-Ru surpass that of many state-of-the-art H<sub>2</sub> evolution systems based on transition metal sulfide photocatalysts, as illustrated in Fig. 3d and detailed in Table S3. Upon Xe lamp illumination, rapid bubble formation was observed within seconds (Fig. S19), indicating the high efficiency of photocatalytic H<sub>2</sub> production coupled with hydrazine oxidation. Gas chromatography analysis of reaction products (Fig. S20) confirmed the exclusive formation of H<sub>2</sub> and N<sub>2</sub>, with no detectable byproducts.<sup>42</sup> The measured molar ratio of N<sub>2</sub> to H<sub>2</sub> was ca. 1:2, consistent with the complete oxidation of hydrazine. These results collectively highlight the excellent photocatalytic performance and practical applicability of the CdS-Ru system for sustainable hydrogen production.

Building on the prominent photocatalytic H<sub>2</sub> evolution performance of the current reaction system, hydrazine-assisted CO<sub>2</sub> photoreduction was subsequently evaluated. As shown in Fig. 3e, CdS alone produced CH<sub>3</sub>OH (0.11 mmol·g<sup>-1</sup> h<sup>-1</sup>), CO (0.04 mmol·g<sup>-1</sup> h<sup>-1</sup>), and H<sub>2</sub> (0.12 mmol·g<sup>-1</sup> h<sup>-1</sup>), resulting in a relatively low CH<sub>3</sub>OH selectivity of 77.3 %. In contrast, CdS-Ru exhibited significantly enhanced performance, producing CH<sub>3</sub>OH at 1.4 mmol·g<sup>-1</sup> h<sup>-1</sup> and H<sub>2</sub> at 1.2 mmol·g<sup>-1</sup> h<sup>-1</sup>, with a CH<sub>3</sub>OH selectivity of 99.0 % and AQE of 0.12% at 420 nm. Although current CO<sub>2</sub> reduction reaction system still suffers from the competitive H<sub>2</sub> evolution reaction, the markedly improved CH<sub>3</sub>OH production rate and selectivity are superior to most reported data (Fig. 3d and Table S4).

Nuclear magnetic resonance (NMR) spectroscopy (Fig. 3f) confirmed that no other carbonaceous (C-N coupling) or NH<sub>3</sub> products were present in the liquid phase, supporting the conclusion that CH<sub>3</sub>OH and H<sub>2</sub> are the dominant products. Notably, replacing hydrazine with a conventional scavenger such as TEOA or Na<sub>2</sub>S/Na<sub>2</sub>SO<sub>3</sub> led to a dramatic decline in photocatalytic activity, with CH<sub>3</sub>OH becoming nearly undetectable (Fig. 3g). This pronounced difference is likely due to the low oxidation potential of hydrazine, which not only facilitates efficient separation of photoexcited charge carriers but also helps prevent overoxidation of CH<sub>3</sub>OH, thereby enhancing product yield and selectivity.<sup>45</sup> The stability of CH<sub>3</sub>OH

production was also evaluated, with five consecutive cycles (25 h total) showing negligible activity loss (Fig. S21), confirming the excellent durability of CdS-Ru for CO<sub>2</sub> photoreduction.

To verify the origin of the products generated during solar fuel production, isotopic labeling experiments were conducted using <sup>13</sup>CO<sub>2</sub> and/or D<sub>2</sub>O as reactants. The resulting products were analyzed via gas chromatography-mass spectrometry (GC-MS). As shown in Fig. S22, when the <sup>13</sup>CO<sub>2</sub> was used as the carbon source, the main mass fragment appeared at *m/z* = 33, corresponding to <sup>13</sup>CH<sub>3</sub>OH, confirming that the carbon in methanol originates from CO<sub>2</sub>. When H<sub>2</sub>O was further replaced with D<sub>2</sub>O, the primary signal shifted to *m/z* = 37, consistent with the molecular weight of <sup>13</sup>CD<sub>3</sub>OD, indicating that the hydrogen in methanol is derived from water. In addition, the H<sub>2</sub> signal shifted to *m/z* = 4, confirming the formation of isotopically labeled D<sub>2</sub> gas. These results unambiguously demonstrate that the C in CH<sub>3</sub>OH originates from CO<sub>2</sub>, while the H in both H<sub>2</sub> and CH<sub>3</sub>OH is sourced from H<sub>2</sub>O, confirming the true solar-to-fuel conversion pathway.

### 3.3 Mechanism of photocatalytic performance enhancement

We next investigated the origin of the enhanced photocatalytic performance and the underlying reaction mechanism for solar fuel production coupled with hydrazine degradation. First, the optical absorption capacities of CdS and CdS-Ru were analyzed using ultraviolet-visible diffuse reflectance spectroscopy (UV-vis DRS). As shown in Fig. 4a, both materials exhibit similar optical bandgaps, indicating that Ru incorporation does not significantly alter the band structure of CdS. However, CdS-Ru displays a notably higher photoabsorption intensity compared to pristine CdS. While increasing the Ru content further enhances the absorption intensity (Fig. S23), it does not result in a corresponding improvement in photocatalytic activity. This observation suggests that the superior performance of CdS-Ru cannot be attributed solely to increased light absorption due to Ru incorporation. Therefore, other factors, such as improved charge separation, interfacial charge transfer, and catalytic site efficiency, likely play a more critical role in the observed enhancement.

To gain further insight into the enhanced photocatalytic performance, we investigated the charge carrier dynamics. Photoluminescence (PL) spectroscopy revealed that CdS-Ru exhibits a significantly lower PL intensity compared to pristine CdS (Fig. 4b and Fig. S24), indicating reduced radiative recombination of photoexcited charge carriers upon Ru loading. However, a high fraction of Ru incorporation can also lead to charge carrier recombination and result in decreased photocatalytic performance.<sup>31</sup> Time-resolved PL (TR-PL) spectroscopy with excitation at 400 nm and probe at 530 nm was then employed to quantify the charge carrier lifetimes (Fig. 4c). Based on the fitted results (Table S5), the average lifetime of charge carriers in CdS-Ru was found to be 2.71 ns, substantially longer than that of CdS (1.51 ns). This prolongation suggests more efficient charge separation and slower recombination processes in CdS-Ru sample. Furthermore, electrochemical impedance spectroscopy (EIS) was performed



at reducing potentials of 0.3 V, -0.8 V and -0.9 V, with the results shown in Fig. 4d and Fig. S25. CdS-Ru exhibits a consistently smaller semicircle diameter than CdS at both potentials, indicating lower charge transfer resistance and more efficient charge separation, which is in good agreement with the PL result in Figs. 4b. Moreover, as the applied potential becomes more extreme, the impedance of both electrodes decreases significantly, consistent with the trend reported.<sup>46,47</sup> Consistently, CdS-Ru displayed the highest photocurrent density among the samples (Fig. 4e), further confirming

improved photoinduced charge separation and mobility. Generally, a larger potential difference ( $\Delta E_{ph}$ ) during light on/off indicates a higher accumulation of electrons. Therefore, the higher  $\Delta E_{ph}$  of CdS-Ru can be attributed to the promotion of charge separation efficiency, which leads to a higher photovoltage (Fig. 4f). Collectively, these results demonstrate that the incorporation of atomically dispersed Ru sites facilitates more efficient charge transfer and separation, thereby contributing to the superior photocatalytic activity of the CdS-Ru system.<sup>48</sup>

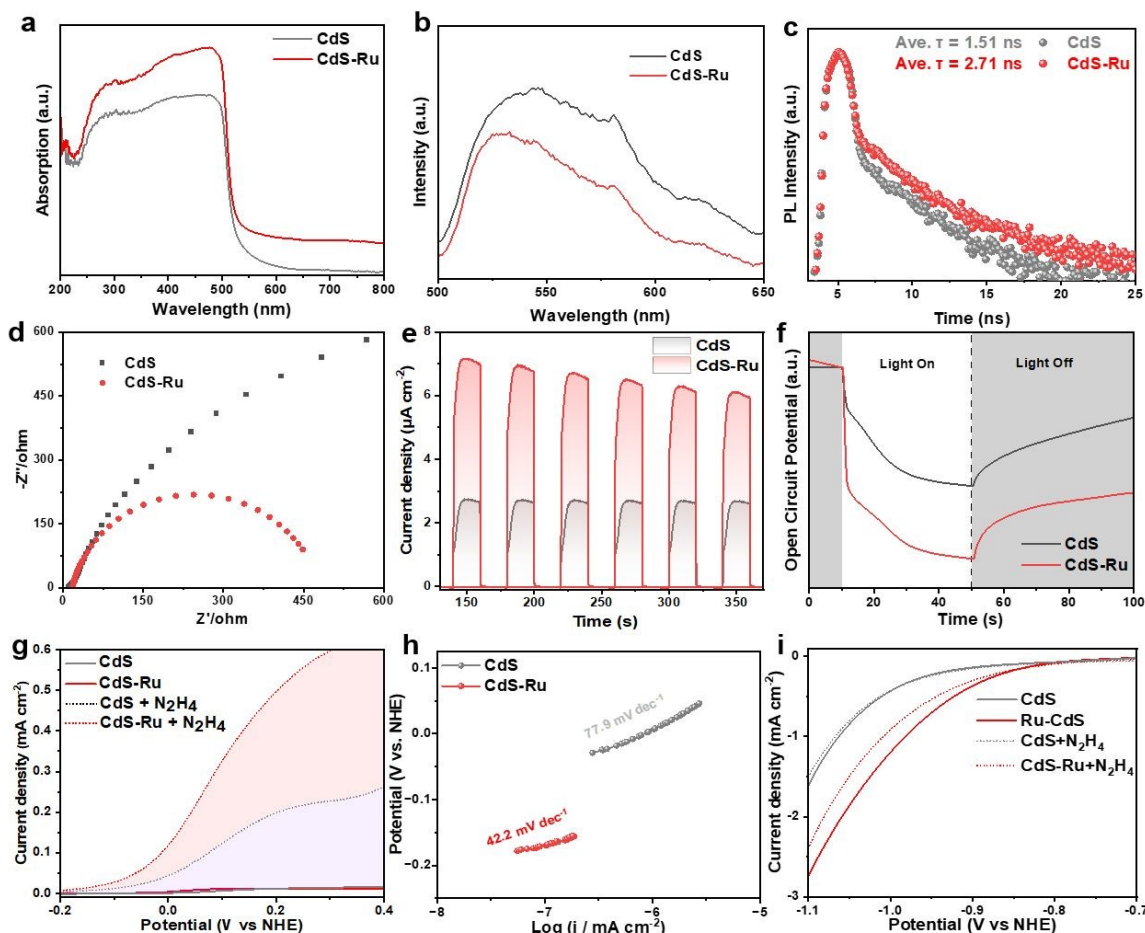


Fig. 4. (a) UV-vis DRS spectra, (b) PL spectra, (c) TR-PL spectra upon excitation at 400 nm, (d) EIS spectra tested at -0.8 V, (e) transient photocurrent response curves and (f) open-circuit voltage of CdS-Ru and CdS under a Xe lamp ( $200 \text{ mW cm}^{-2}$ ,  $\lambda > 420 \text{ nm}$ ) irradiation. (g) LSV curves and (h) Tafel slope of CdS and CdS-Ru for  $\text{H}_2\text{O}$  or  $\text{N}_2\text{H}_4$  oxidation. (i) LSV curves of CdS and CdS-Ru for proton reduction.

To further elucidate the roles of Ru sites and hydrazine oxidation in influencing the kinetics of solar fuel production, linear sweep voltammetry (LSV) measurements were conducted. As shown in Fig. 4g, both CdS and CdS-Ru electrodes exhibit minimal current densities in 0.5 M  $\text{Na}_2\text{SO}_4$  electrolyte without hydrazine, due to the high overpotential and sluggish kinetics associated with  $\text{H}_2\text{O}$  oxidation.<sup>49, 50</sup> Upon the introduction of 1 mM hydrazine into the electrolyte, a sharp rise in responsive current is observed for both materials, with CdS-Ru showing a notably higher response than CdS. For example, at 0.1 V, CdS-Ru achieves a current density of  $0.32 \text{ mA cm}^{-2}$ , approximately 3 times greater than CdS ( $0.11 \text{ mA cm}^{-2}$ ) and 32 times higher than CdS-Ru in the absence of hydrazine ( $0.01 \text{ mA}$

$\text{cm}^{-2}$ ). Tafel slope analysis was used to evaluate the kinetic behavior of the hydrazine oxidation reaction (HzOR). As presented in Fig. 4h, the Tafel slope for CdS-Ru is  $42.2 \text{ mV dec}^{-1}$ , significantly lower than that of CdS ( $77.9 \text{ mV dec}^{-1}$ ), indicating more favorable HzOR kinetics.<sup>50</sup> These results strongly suggest that the atomically dispersed Ru sites act as the primary active centers for promoting HzOR.<sup>51</sup>

The kinetics of the reduction half-reaction were also studied using LSV technology. As shown in Fig. 4i, the CdS-Ru electrode shows a reduced overpotential for  $\text{H}_2$  evolution in comparison with pristine CdS, which correlates with the increased  $V_s$  density in CdS-Ru, as summarized in Table S6. This enhancement indicates that  $V_s$  and Ru sites contribute to improved catalytic



activity for proton reduction. Despite the lower overpotential, the Tafel slope of CdS-Ru remains comparable to that of CdS (Fig. S26), manifesting that the rate-determining step is still governed by surface adsorption/desorption processes, rather than charge transfer kinetics.<sup>22</sup> Interestingly, upon the addition of hydrazine into the Na<sub>2</sub>SO<sub>4</sub> electrolyte, the current density of CdS-Ru decreases significantly, while that of CdS remains largely unaffected, which competitively inhibits the adsorption and reduction of protons.<sup>52</sup> This interaction and its mechanisms will be further elucidated through density functional theory (DFT) calculations in subsequent sections.

### 3.4 DFT calculations and in situ FTIR analysis

Density functional theory (DFT) calculations were performed to explore the electronic structure modifications induced by V<sub>s</sub> and atomically dispersed Ru sites in the catalyst. All structural models were fully optimized, with the resulting geometries presented in Fig. S27. The optimized structure of CdS-Ru shows notable lattice distortions, attributed to the synergistic regulation of both atomic Ru and V<sub>s</sub> sites. These computational results are consistent with experimental observations from XRD and ESR analyses. Density of states (DOS) analysis (Fig. 5a)

reveals the emergence of mid-gap states near the Fermi level upon the incorporation of Ru and V<sub>s</sub>, which are expected to enhance electrical conductivity and promote the separation of photogenerated electron-hole pairs.<sup>53</sup> Furthermore, the d-band center ( $\epsilon_d$ ) of CdS-Ru (3.28 eV) is shifted downward relative to that of CdS (3.47 eV), indicating an increased affinity for reactant adsorption, an effect corroborated by the adsorption energy ( $E_{\text{ads}}$ ) calculations. As shown in Fig. 5b, hydrazine molecules interact with CdS and CdS-Ru through Cd-N and Ru-N bonding, yielding  $E_{\text{ads}}$  values of -1.42 eV and -1.47 eV, respectively. The more negative  $E_{\text{ads}}$  on CdS-Ru reflect stronger adsorption strength, which supports the experimentally observed complete oxidation of hydrazine on this catalyst. Similar trends were observed in the case of CO<sub>2</sub> adsorption. As depicted in Fig. 5c, CO<sub>2</sub> is only physically adsorbed on CdS, with a weakly positive  $E_{\text{ads}}$  of +0.47 eV. In contrast, on CdS-Ru, CO<sub>2</sub> undergoes significant molecular activation, as evidenced by bending and elongation of the O=C=O bond. The optimized structure shows that CO<sub>2</sub> is chemically adsorbed via two Cd atoms adjacent to the Ru and V<sub>s</sub> sites, with an  $E_{\text{ads}}$  of -0.33 eV. These results further confirm the enhanced reactivity and activation capability of the CdS-Ru catalyst toward CO<sub>2</sub>.

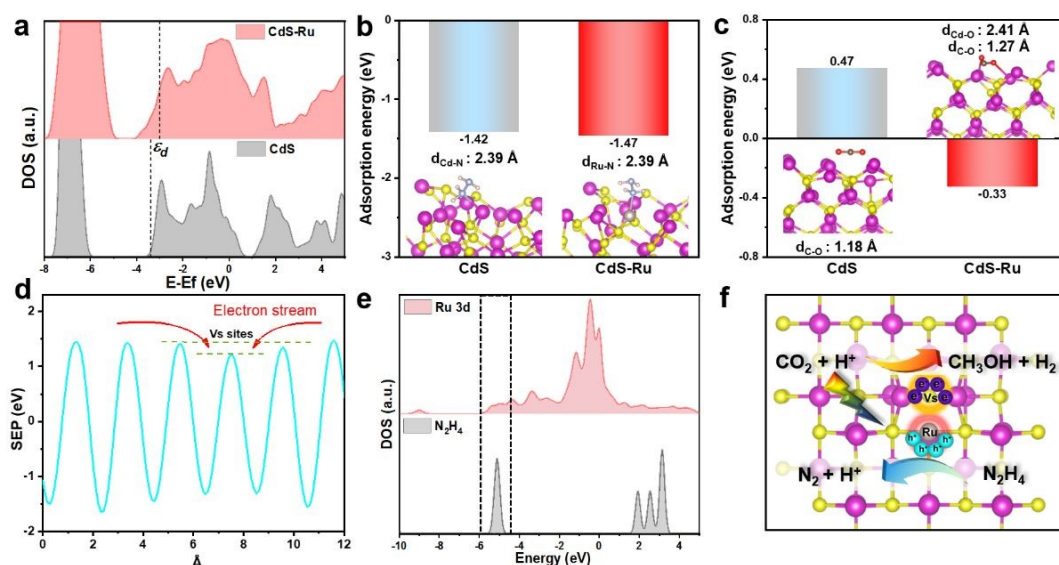


Fig. 5. (a) DOS and d-band center analysis on CdS-Ru and CdS. Adsorption energy of (b) N<sub>2</sub>H<sub>4</sub> and (c) CO<sub>2</sub> on the CdS-Ru and CdS derived from DFT calculations. (d) Surface electrostatic potential on the S facet of CdS-Ru. (e) Comparison of projected DOS of Ru 3d in CdS-Ru and total DOS of N<sub>2</sub>H<sub>4</sub>. (f) Schematic illustration of charge transfer and solar fuel production coupled with hydrazine oxidation over CdS-Ru.

The direction of electron transfer and the site-specific charge accumulation behavior were further explored through surface electrostatic potential mapping (Fig. 5d). The analysis reveals that the V<sub>s</sub> serves as an electron sink, directing the flow of electrons and inducing the redistribution of charge density. This results in localized electron accumulation on the surrounding Cd atoms (Fig. S28), which is beneficial for facilitating reduction reactions in solar fuel production. DOS calculations for hydrazine show a wide energy gap of ca. 7.5 eV, with the highest occupied molecular orbital (HOMO) located at about -5.1 eV (Fig. 5e). This HOMO level closely aligns with the valence band (VB) position of CdS (Fig. S29), suggesting the thermodynamic

feasibility of hole transfer from CdS to hydrazine. Projected DOS analysis of CdS-Ru shows that Ru atoms contribute to the valence band maximum (VBM), implying that Ru sites are capable of accepting photoinduced holes from the CdS semiconductor.<sup>54</sup> Furthermore, there is a clear overlap between the DOS of hydrazine and the Ru 3d orbitals in CdS-Ru within the energy range corresponding to the HOMO of hydrazine (Fig. 5e). This suggests a favorable orbital interaction, enabling efficient hole transfer from photoexcited CdS-Ru to hydrazine via the Ru sites. Controlled experiment in the presence of KBrO<sub>3</sub> as the electron scavenger shows that only N<sub>2</sub> was produced from the hole oxidation of hydrazine (Fig. S30). Based on these



findings, a comprehensive mechanism for charge carrier transfer and the associated redox reactions is proposed in Fig. 5f. The diagram highlights the critical roles of  $V_s$  and atomically dispersed Ru sites in facilitating spatially separated charge transfer, promoting hydrazine oxidation and  $\text{CO}_2$  (or  $\text{H}^+$ ) reduction. This cooperative interaction highlights the chemical synergy essential for boosting solar fuel production.

To elucidate the detailed reaction mechanisms underlying solar fuel production and hydrazine degradation, free energy change ( $\Delta G$ ) calculations were performed. Fig. 6a shows the elementary reaction steps, corresponding energy profiles, and key intermediate configurations for  $\text{CO}_2$  reduction and  $\text{H}_2$  evolution. The  $\text{CO}_2$  reduction pathway begins with the adsorption of  $\text{CO}_2$  as  $^*\text{COOH}$  (where  $*$  denotes an adsorbed species), a well-known, crucial intermediate in  $\text{CO}_2$  conversion. The formation energy of  $\text{COOH}^*$  on CdS-Ru is significantly lower (+0.02 eV) than that on CdS (+0.96 eV), which is attributed to the shift in the d-band center ( $\epsilon_d$ ) induced by Ru incorporation. This reduced energy barrier facilitates the initial  $\text{CO}_2$  activation. Following  $^*\text{COOH}$  formation, the elimination of OH to yield  $^*\text{CO}$  (surface-bound carbonyl) is exothermic on both catalysts. The subsequent transformation of  $^*\text{CO}$  plays a pivotal role in determining the product distribution. For CdS-Ru, the hydrogenation of  $^*\text{CO}$  to  $^*\text{CHO}$  is identified as the rate-determining step, with a  $\Delta G$  of +0.61 eV lower than that of CdS (+0.77 eV). Moreover, the energy barrier for  $^*\text{CO}$  desorption is higher than that for  $^*\text{CHO}$  formation, suggesting that further hydrogenation toward  $\text{CH}_2\text{O}$  species and eventually  $\text{CH}_3\text{OH}$  is more favorable than  $\text{CO}$  adsorption.<sup>55</sup> This explains the

enhanced  $\text{CH}_3\text{OH}$  selectivity observed experimentally (Fig. 3e). In the case of  $\text{H}_2$  evolution, the green energy profile in Fig. 6a shows that CdS-Ru has a lower energy barrier (0.13 eV) compared to CdS (0.20 eV), consistent with LSV results (Fig. 4f). Notably, this moderate energy barrier closely matches that of  $\text{CO}_2$  activation (0.15 eV), enabling concurrent formation of key intermediates for both  $\text{H}_2$  production and  $\text{CO}_2$  reduction, thereby contributing to the observed high activity and selectivity on CdS-Ru. While Ru is often recognized as an effective cocatalyst for water splitting due to its favorable water dissociation kinetics,<sup>17</sup> our calculations reveal a strong  $^*\text{H}$  binding energy on Ru sites (0.74 eV, Fig. S31). This suggests that atomically dispersed Ru acts primarily active sites for HzOR. In summary, the free energy analysis confirms that the enhanced catalytic performance and  $\text{CH}_3\text{OH}$  selectivity of CdS-Ru arise from the favorable energetics of intermediate formation, efficient charge utilization, and the complementary roles of Ru and  $V_s$  in modulating reaction pathways.

The high selectivity toward  $\text{CH}_3\text{OH}$  and the absence of formic acid or formate can be attributed to the favorable energetics of the  $^*\text{CO}$  hydrogenation pathway on CdS-Ru. The  $^*\text{COOH}$  intermediate formed after  $\text{CO}_2$  activation preferentially undergoes dehydration to form  $^*\text{CO}$  rather than protonation to  $\text{HCOOH}$ , and the strongly adsorbed  $^*\text{CO}$  is kinetically driven toward further hydrogenation to  $\text{CH}_3\text{OH}$  rather than desorption as  $\text{CO}$  or formate. This mechanistic preference, governed by the unique electronic structure of the catalyst, steers the  $\text{CO}_2$  reduction pathway exclusively toward  $\text{CH}_3\text{OH}$ .

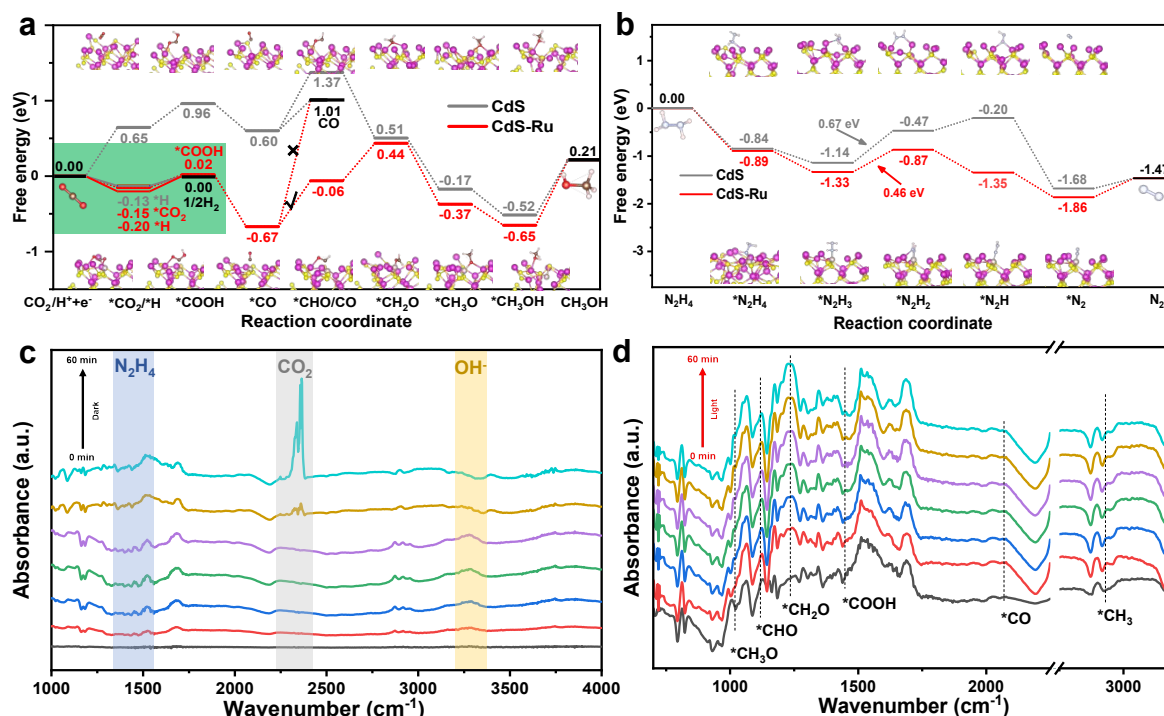


Fig. 6. (a) Free energy profiles for the  $\text{H}_2$  evolution and  $\text{CO}_2$  reduction over CdS-Ru and CdS. (b) Free energy profiles of  $\text{N}_2\text{H}_4$  dehydrogenation/oxidation over CdS-Ru and CdS. The insets of (a) and (b) show the corresponding structure models. In situ FT-IR spectra for co-adsorption of  $\text{N}_2\text{H}_4$  and  $\text{CO}_2$  on CdS-Ru (c) in the dark and (d) under visible light irradiation.

Given the limited research on hydrazine degradation over the photocatalysts,<sup>19, 56, 57</sup> it is essential to develop a deeper

mechanistic understanding of dehydrogenation/oxidation kinetics of hydrazine. The reaction pathways for hydrazine



degradation on CdS and CdS-Ru are demonstrated in Fig. 6b. Overall, the hydrazine degradation process is thermodynamically favorable and proceeds spontaneously in both systems. However, a key difference lies in the rate-determining step: the dehydrogenation of  $^*N_2H_3$  to  $^*N_2H_2$ . This step presents an energy barrier of 0.46 eV on CdS-Ru, which is significantly lower than the 0.67 eV barrier observed on pristine CdS. Beyond this step, all subsequent elementary reactions on CdS-Ru are also exergonic, facilitating the complete multi-step dehydrogenation of hydrazine to  $N_2$ . In contrast, the CdS catalyst encounters an additional energy barrier of 0.27 eV during the conversion of  $^*N_2H_2$  to the next intermediate, further hindering the overall reaction kinetics. These findings highlight the critical role of atomically dispersed Ru sites in lowering kinetic barriers and promoting efficient, stepwise hydrazine dehydrogenation/oxidation. Together, these mechanistic insight highlights the catalytic advantage of CdS-Ru in enabling the complete and selective conversion of hydrazine to nitrogen, reinforcing its potential for use in photocatalytic pollutant degradation and solar fuel production.

To further elucidate the distinct roles of Ru and sulfur vacancies, we combined electronic structure analysis with reaction energy profiles. Surface electrostatic potential mapping (Fig. 5d) and charge distribution (Fig. S28) reveal that  $V_S$  induces electron accumulation on adjacent Cd atoms, creating reductive centers, while Ru sites exhibit strong orbital hybridization with the HOMO of  $N_2H_4$  (Fig. 5e) and significantly lower the dehydrogenation barrier (Fig. 6b), confirming their function as oxidative centers. Moreover,  $^*H$  adsorption on Ru is unfavorable (0.74 eV, Fig. S31), and  $^*COOH$  formation, the key step in  $CO_2$  reduction, occurs on Cd rather than Ru (Fig. 6a). These findings demonstrate a spatial separation of redox functions that Ru sites accelerate hydrazine oxidation, whereas electron-rich Cd sites adjacent to  $V_S$  promote  $CO_2$  reduction and  $H_2$  evolution. This synergistic cooperation underpins the high efficiency of the CdS-Ru system.

Finally, in situ FTIR spectra tests were conducted to confirm the proposed reaction pathway and intermediates.  $CO_2$  and  $N_2H_4$  were purged into the system in the dark, and the spectra were collected every 10 min. The accumulated intermediate species adsorbed on the surface of CdS-Ru can be identified from Fig. 6c. The bands in the range of 1300-1500  $cm^{-1}$  indicate that the adsorption of  $N_2H_4$  is associated with the wagging vibrational mode of the  $-NH_2$  group in  $N_2H_4$ .<sup>58</sup> The peaks at approximately 2340 and 2360  $cm^{-1}$  correspond to the adsorbed  $CO_2$  on the surface of the catalyst.<sup>59</sup> The characteristic peaks of the adsorbed  $N_2H_4$  and  $CO_2$  are gradually enhanced, which leads to the intensity of surface  $OH^-$  species first increase, followed by a gradual decrease. This suggests that the presence of  $N_2H_4$  may create more surface alkaline sites to promote the chemical adsorption of  $CO_2$ . Then the spectral signals under visible light irradiation were recorded with time interval of 10 min. As illustrated in Fig. 6d, new peaks attributed to reaction intermediates are emerged after light irradiation. The absorption bands of  $^*COOH$  intermediate appear in the range of 1440-1460  $cm^{-1}$ .<sup>59</sup> The linearly adsorbed  $^*CO$  intermediate can be identified via the band at 2060  $cm^{-1}$ .<sup>60</sup> The band at 1140

$cm^{-1}$  corresponds to the characteristic peak of  $^*CHO$ .<sup>60</sup> The characteristic band appearing at 1240  $cm^{-1}$  is assigned to  $^*CH_2O$ , while the band at 1020  $cm^{-1}$  and 2960  $cm^{-1}$  belong to the characteristic peak of  $^*CH_3O$  and  $^*CH_3$ , which are the crucial intermediate for  $CO_2$  reduction to methanol.<sup>59-61</sup> With the extension of irradiation time, the intensity of each characteristic peak gradually increased indicating the gradually hydrogenation of  $CO_2$  to generate methanol. The key redox steps for the catalytic system were summarized in Equations S1-S6.

## 4. Conclusions

In summary, we report the first successful integration of atomically dispersed Ru sites into CdS with  $V_S$  and systematically elucidate their structural and catalytic roles in solar fuel production coupled with hydrazine degradation. The synergistic presence of atomic Ru and  $V_S$  enables regional and directional separation of photoexcited charge carriers, driving oxidative reactions at Ru sites and reductive reactions at adjacent regions, thereby enhancing overall catalytic efficiency. Employing hydrazine as a hole scavenger not only circumvents the sluggish kinetics associated with water oxidation but also eliminates carbon emissions, making the process environmentally benign. Owing to this dual-site and chemical synergy, the CdS-Ru system demonstrates significantly improved photocatalytic activity for both  $H_2$  evolution and  $CO_2$  reduction to  $CH_3OH$ , while achieving complete oxidation of toxic hydrazine to  $N_2$ . This work offers valuable insights into the rational design of multifunctional photocatalysts and integrated reaction strategies for achieving efficient solar fuel production with added environmental benefits, paving the way for sustainable and clean energy technologies.

## Author contributions

Zikang Zeng: Writing – original draft, Methodology, Investigation, Data curation, Conceptualization. Siyu Kang: Methodology, Data curation. Xiaohe Jiang: Methodology, Conceptualization. Hai Qiu: Formal analysis. Yu-Chia Chang: Visualization, Investigation. Yu-Ting Chueh: Data curation. Lan Yuan: Writing – review & editing, Investigation. Yujun Liang: Visualization, Investigation. Jianguo Chang: Methodology, Funding acquisition. Gui Yang: Supervision, Resources. Sung-Fu Hung: Writing – review & editing, Visualization, Investigation, Funding acquisition. Chuang Han: Writing – review & editing, Supervision, Resources, Funding acquisition.

## Conflicts of interest

There are no conflicts to declare.

## Data availability

The data supporting this article have been included as part of the Supplementary Information. Supplementary information: Tables S1-



S6, Figures S1-S28, DFT computational method and further experimental details. See DOI: [URL – format <https://doi.org/DOI>]

## Acknowledgements

The supports from the National Natural Science Foundation of China (52572329, 22302182, 22102126), the Natural Science Foundation of Hubei Province (2023AFB091), the “CUG Scholar” Scientific Research Funds at China University of Geosciences (Wuhan) (Project No.2022187), the Key Research Project of the Anhui Provincial Key Laboratory of Green Carbon Chemistry (AHGC2025005), and the National Science and Technology Council, Taiwan (Contract No. NSTC 113-2628-M-A49-008) are gratefully acknowledged. We also thank Dr. Mingxing Gong for STEM characterizations and discussions, and the support from the Yushan Young Scholar Program and the Center for Emergent Functional Matter Science, Ministry of Education, Taiwan.

## References

- J. Tian, Y. Zhang, L. Du, Y. He, X.-H. Jin, S. Pearce, J.-C. Eloi, R. L. Harniman, D. Alibhai and R. Ye, *Nat. Chem.*, 2020, **12**, 1150-1156.
- X. Li, Y. Sun, J. Xu, Y. Shao, J. Wu, X. Xu, Y. Pan, H. Ju, J. Zhu and Y. Xie, *Nat. Energy*, 2019, **4**, 690-699.
- H. Zhang, Y. Wang, S. Zuo, W. Zhou, J. Zhang and X. W. D. Lou, *J. Am. Chem. Soc.*, 2021, **143**, 2173-2177.
- M. Z. Rahman, T. Edvinsson and J. Gascon, *Nat. Rev. Chem.*, 2022, **6**, 243-258.
- S. Lin, Y. Zhang, Y. You, C. Zeng, X. Xiao, T. Ma and H. Huang, *Adv. Funct. Mater.*, 2019, **29**, 1903825.
- W. Wang, Y. Tao, J. Fan, Z. Yan, H. Shang, D. L. Phillips, M. Chen and G. Li, *Adv. Funct. Mater.*, 2022, **32**, 2201357.
- K. Doudrick, T. Yang, K. Hristovski and P. Westerhoff, *Appl. Catal. B-Environ.*, 2013, **136**, 40-47.
- H. Xu, X. She, T. Fei, Y. Song, D. Liu, H. Li, X. Yang, J. Yang, H. Li and L. Song, *ACS nano*, 2019, **13**, 11294-11302.
- K. Iwashina, A. Iwase, Y. H. Ng, R. Amal and A. Kudo, *J. Am. Chem. Soc.*, 2015, **137**, 604-607.
- S. Wang, T. Wu, S. Wu, J. Guo, T. He, Y. Wu, W. Yuan, Z. Zhang, Y. Hua and Y. Zhao, *Angew. Chem. Int. Ed.*, 2023, **62**, e202311082.
- J. Lin, Y. Wang, W. Tian, H. Zhang, H. Sun and S. Wang, *ACS Catal.*, 2023, **13**, 11711-11722.
- H. Wen, L.-Y. Gan, H.-B. Dai, X.-P. Wen, L.-S. Wu, H. Wu and P. Wang, *Appl. Catal. B-Environ.*, 2019, **241**, 292-298.
- J. Carvalho Jr, C. Bressan and J. Ferreira, *Energy*, 1988, **13**, 149-152.
- C. Feng, M. Lv, J. Shao, H. Wu, W. Zhou, S. Qi, C. Deng, X. Chai, H. Yang and Q. Hu, *Adv. Mater.*, 2023, **35**, 2305598.
- A. U. Nwankwoala, N. O. Egiebor and K. Nyavor, *Biodegradation*, 2001, **12**, 1-10.
- Y.-y. Li, L. Lin, X. Huang and X.-y. Li, *Chem. Eng. J.*, 2023, **470**, 144268.
- J. Li, Y. Li, J. Wang, C. Zhang, H. Ma, C. Zhu, D. Fan, Z. Guo, M. Xu and Y. Wang, *Adv. Funct. Mater.*, 2022, **32**, 2109439.
- X. Fu, D. Cheng, C. Wan, S. Kumari, H. Zhang, A. Zhang, H. Huyan, J. Zhou, H. Ren and S. Wang, *Adv. Mater.*, 2023, **35**, 2301533.
- Y. Hu, T. Chao, Y. Li, P. Liu, T. Zhao, G. Yu, C. Chen, X. Liang, H. Jin and S. Niu, *Angew. Chem. Int. Ed.*, 2023, **135**, e202308800.
- W. Zhu, A. G. Naidu, Q. Wu, H. Yan, M. Zhao, Z. Wang and H. Liang, *Chem. Eng. Sci.*, 2022, **258**, 117769.
- H.-C. Eun, J.-Y. Jung, S.-Y. Park, J.-S. Park, N.-O. Chang, S.-B. Kim and B.-K. Seo, *Int. J. Environ. Res.*, 2020, **14**, 385-391.
- J. Li, Y. Li, J. Wang, C. Zhang, H. Ma, C. Zhu, D. Fan, Z. Guo, M. Xu, Y. Wang and H. Ma, *Adv. Funct. Mater.*, 2022, **32**, 2109439.
- Y. Liu, J. Zhang, Y. Li, Q. Qian, Z. Li, Y. Zhu and G. Zhang, *Nat. Commun.*, 2020, **11**, 1853.
- Q. Qian, J. Zhang, J. Li, Y. Li, X. Jin, Y. Zhu, Y. Liu, Z. Li, A. El - Harairy and C. Xiao, *Angew. Chem. Int. Ed.*, 2021, **133**, 6049-6058.
- R. Das, S. Chakraborty and S. C. Peter, *ACS Energy Lett.*, 2021, **6**, 3270-3274.
- C. Hu, Y. Zhang, A. Hu, Y. Wang, X. Wei, K. Shen, L. Chen and Y. Li, *Adv. Mater.*, 2023, **35**, 2209298.
- X. Guan, Q. Wu, H. Li, S. Zeng, Q. Yao, R. Li, H. Chen, Y. Zheng and K. Qu, *Appl. Catal. B-Environ.*, 2023, **323**, 122145.
- D. Liu, T. Ding, L. Wang, H. Zhang, L. Xu, B. Pang, X. Liu, H. Wang, J. Wang and K. Wu, *Nat. Commun.*, 2023, **14**, 1720.
- X. Li, W. Bi, L. Zhang, S. Tao, W. Chu, Q. Zhang, Y. Luo, C. Wu and Y. Xie, *Adv. Mater.*, 2016, **28**, 2427-2431.
- X. Shi, C. Dai, X. Wang, J. Hu, J. Zhang, L. Zheng, L. Mao, H. Zheng and M. Zhu, *Nat. Commun.*, 2022, **13**, 1287.
- N. Luo, T. Montini, J. Zhang, P. Fornasiero, E. Fonda, T. Hou, W. Nie, J. Lu, J. Liu, M. Heggen, L. Lin, C. Ma, M. Wang, F. Fan, S. Jin and F. Wang, *Nat. Energy*, 2019, **4**, 575-584.
- S. Zhang, Z. Zhang, Y. Si, B. Li, F. Deng, L. Yang, X. Liu, W. Dai and S. Luo, *ACS nano*, 2021, **15**, 15238-15248.
- J. Wang, C. Yang, L. Mao, X. Cai, Z. Geng, H. Zhang, J. Zhang, X. Tan, J. Ye and T. Yu, *Adv. Funct. Mater.*, 2023, **33**, 2213901.
- Y. Cao, L. Guo, M. Dan, D. E. Doronkin, C. Han, Z. Rao, Y. Liu, J. Meng, Z. Huang and K. Zheng, *Nat. Commun.*, 2021, **12**, 1675.
- Y. Cao, L. Guo, M. Dan, D. E. Doronkin, C. Han, Z. Rao, Y. Liu, J. Meng, Z. Huang, K. Zheng, P. Chen, F. Dong and Y. Zhou, *Nat. Commun.*, 2021, **12**, 1675.
- S. Liu, N. Zhang, Z.-R. Tang and Y.-J. Xu, *ACS Appl. Mater. Interfaces*, 2012, **4**, 6378-6385.
- Y. Wang, X. Liu, X. Han, R. Godin, J. Chen, W. Zhou, C. Jiang, J. F. Thompson, K. B. Mustafa and S. A. Shevlin, *Nat. Commun.*, 2020, **11**, 2531.
- Y. Li, T. Qin, Y. Wei, J. Xiong, P. Zhang, K. Lai, H. Chi, X. Liu, L. Chen and X. Yu, *Nat. Commun.*, 2023, **14**, 7149.
- A. Talebian-Kiakalaieh, M. Guo, E. M. Hashem, B. Xia, Y. Jiang, C. Chuah, Y. Tang, P. Kwong, J. Ran and S.-Z. Qiao, *Adv. Energy Mater.*, 2023, **13**, 2301594.
- B. Zhu, J. Sun, Y. Zhao, L. Zhang and J. Yu, *Adv. Mater.*, 2024, **36**, 2310600.
- W. Li, X. Zheng, B. B. Xu, Y. Yang, Y. Zhang, L. Cai, Z. J. Wang, Y. F. Yao, B. Nan and L. Li, *Angew. Chem. Int. Ed.*, 2024, e202320014.
- H. Peng, T. Yang, H. Lin, Y. Xu, Z. Wang, Q. Zhang, S. Liu, H. Geng, L. Gu and C. Wang, *Adv. Energy Mater.*, 2022, **12**, 2201688.
- H. M. Wasana, G. D. Perera, P. D. S. Gunawardena, P. S. Fernando and J. Bandara, *Sci. Rep.*, 2017, **7**, 42516.
- Y. Wang, Y. Wang and R. Xu, *J. Phys. Chem. C*, 2013, **117**, 783-790.
- P. Wang, J. Zheng, X. Xu, Y. Q. Zhang, Q. F. Shi, Y. Wan, S. Ramakrishna, J. Zhang, L. Zhu and T. Yokoshima, *Adv. Mater.*, 2024, **36**, 2404806.
- J. Jia, D. Li, X. Cheng, J. Wan and X. Yu, *Appl. Catal. A: Gen.*, 2016, **525**, 128-136.
- S. Zhan, F. Zhou, N. Huang, Y. Liu, Q. He, Y. Tian, Y. Yang and F. Ye, *Appl. Surf. Sci.*, 2017, **391**, 609-616.
- H.-W. Tseng, M. B. Wilker, N. H. Damrauer and G. Dukovic, *J. Am. Chem. Soc.*, 2013, **135**, 3383-3386.



## COMMUNICATION

Journal Name

49. J. Guan, K. Koizumi, N. Fukui, H. Suzuki, K. Murayama, R. Toyoda, H. Maeda, K. Kamiya, K. Ohashi and S. Takaishi, *ACS Catal.*, 2024, **14**, 1146-1156.
50. R. Yin, Z. Wang, J. Zhang, W. Liu, J. He, G. Hu and X. Liu, *Small Methods*, 2025, **9**, 2401976.
51. B. Yan, D. Liu, X. Feng, M. Shao and Y. Zhang, *Adv. Funct. Mater.*, 2020, **30**, 2003007.
52. Y. Zhu, Y. Chen, Y. Feng, X. Meng, J. Xia and G. Zhang, *Adv. Mater.*, 2024, **36**, 2401694.
53. A. Mukherji, R. Marschall, A. Tanksale, C. Sun, S. C. Smith, G. Q. Lu and L. Wang, *Adv. Funct. Mater.*, 2011, **21**, 126-132.
54. A. Talebian - Kiakalaieh, M. Guo, E. M. Hashem, B. Xia, Y. Jiang, C. Chuah, Y. Tang, P. Kwong, J. Ran and S. Z. Qiao, *Adv. Energy Mater.*, 2023, **13**, 2301594.
55. Y. Hu, T. Chao, Y. Dou, Y. Xiong, X. Liu and D. Wang, *Adv. Mater.*, 2025, 2418504.
56. Q. Kang, T. Wang, P. Li, L. Liu, K. Chang, M. Li and J. Ye, *Angew. Chem. Int. Ed.*, 2015, **54**, 841-845.
57. J. Wang, X. Guan, H. Li, S. Zeng, R. Li, Q. Yao, H. Chen, Y. Zheng and K. Qu, *Nano Energy*, 2022, **100**, 107467.
58. C. Wang, J. Li, Y. Yuan, B. Ouyang, Z. Guo, C. Lin, X. Yang, B. Kang, C. Li, Y. Sun and K. Xu, *Angew. Chem. Int. Ed.*, 2025, **64**, e202505616.
59. H. Yu, Y. Xuan, Q. Zhu and S. Chang, *Green Chem.*, 2023, **25**, 596-605.
60. J. Li, W. Pan, Q. Liu, Z. Chen, Z. Chen, X. Feng and H. Chen, *J. Am. Chem. Soc.*, 2021, **143**, 6551-6559.
61. X. Li, L. Li, G. Chen, X. Chu, X. Liu, C. Naisa, D. Pohl, M. Löffler and X. Feng, *Nature Commun.*, 2023, **14**, 4034.

View Article Online  
DOI: 10.1039/D6MH00152A

Open Access Article. Published on 24 April 2026. Downloaded on 4/25/2026 12:04:55 PM.  
This article is licensed under a Creative Commons Attribution-NonCommercial 3.0 Unported Licence.



Materials Horizons Accepted Manuscript